


A new view of the solar atmosphere: daily full-disk multifrequency radio images from EOVS

EOVSA A new view of the solar atmosphere: daily full-disk multifrequency radio images from EOVS

Dale E. Gary, Sijie Yu, Bin Chen, Vito LaVilla
Center for Solar-Terrestrial Research - New Jersey Institute of Technology

1. Overview of EOVS



The Expanded Owens Valley Solar Array

↓

2. Comparison with Previous Work

2.1 Solar Full Disk Imaging Complex from History

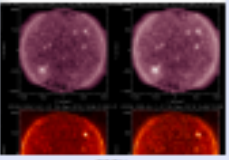
The earliest attempt to define the brightness temperature profile of the quiet Sun was that by Christianus G. Starbuck (1922) at a wavelength of 21 cm (1.4 GHz). The result shown in Figure 2.1, based on multiple aerial-terrestrial scans of the Sun using the solar minimum period (1922-1924) shows remarkably well the main features of extended limb brightening and solar disk dimming.

↓

3. Limb Brightening and Coronal Hole Darkening

3.1 Cross-sectional Profiles

The equatorial regions of the radio images show clear limb brightening, where the edges of the Sun are brighter than the disk center, as is well known since first reported by Christianus G. Starbuck (1922) and further improved upon by several authors including Barnhill et al. (2011). The EOVS images show not only the general effect, but also some irregularities in the detailed structure, which is easier to see when the radio images are compared with a degraded resolution (1.0) image, as in Figure 3.1. Coronal hole (CH) images are available on the EOVS (1.0) image in the lower right.



↓

4. Quantitative Measurement of Physical Parameters

4.1 Brightness Temperature vs. Temperature

In radio astronomy, the main use of the Rayleigh-Jeans regime ($\nu \ll \nu_c$) is to relate the brightness source function in terms of temperature. Thus, in the radio regime brightness, or intensity, can be expressed conveniently as a brightness temperature. However, it is useful to realize the brightness T_B is actually $T_B = T_e \mu$, where μ is the optical depth. The solar corona presents the case of an optically thin source, which is seen against a background atmosphere that is optically thick, but at a much lower temperature. Following Barnhill et al. (2011), we simplify the situation to:

$$T_e = T_c + \mu T_c$$

where T_c is the temperature of the background atmosphere, typically around 10,000 K, and μ is the temperature of the source, at least 1 MK.

4.2 Relating Measured Brightness Temperature to Column Electron Mass Density

↓

5. Calibration and Full Disk Imaging Pipeline

5.1 Imaging with 12 Antennas

Making these full-disk images is not easy with only 12 antennas, but it is greatly helped by a technique called frequency synthesis, and by making the image over an entire 3-hour day while the Earth rotates.

Radio arrays make measurements in spatial Fourier space (called the uv plane), which are then Fourier inverted to form an image of the sky plane.

↓

6. Conclusion

6.1 EOVS Capabilities


The Expanded Owens Valley Solar Array is now producing daily full-disk, multifrequency radio images via its imaging pipeline. This capability is new, and has never been possible before. The spatially-resolved, multi-frequency images reveal the entire range of sources of the solar

↓

Dale E. Gary, Sijie Yu, Bin Chen, Vito LaVilla

Center for Solar-Terrestrial Research – New Jersey Institute of Technology

PRESENTED AT:



AAS 235

235TH MEETING OF THE AMERICAN ASTRONOMICAL SOCIETY

HONOLULU, HAWAII
4-8 JANUARY 2020

Joint with AAS Historical Astronomy and High Energy Astrophysics Divisions

Online poster can be viewed at

<https://aas235-aas.ipostersessions.com/default.aspx?s=97-69-9E-4B-34-19-68-53-1B-C6-21-0C-16-1C-5C-82&guestview=true>

1. OVERVIEW OF EOVSVA



The *Expanded Owens Valley Solar Array (EOVSA)* is a solar-dedicated imaging array of 13 2.1-m antennas operating in the microwave range 1-18 GHz. It covers this wide frequency range at a cadence of 1 s, producing 451 science frequency channels covering 50 bands of 325 MHz bandwidth. Imaging at this high frequency- and time-resolution is essential to follow the spatial, spectral, and temporal evolution of flaring emission produced by high-energy electrons in solar flares.

This talk focuses on a different aspect of solar activity, full-disk images at 6 standard frequency ranges integrated over an entire (typically 8-hour) day. Such long integrations are needed to image the complex solar brightness distribution using only 13 antennas. We are now in a period of extreme solar minimum, yet the EOVSVA images show a startlingly clear and complex array of quiet Sun features.

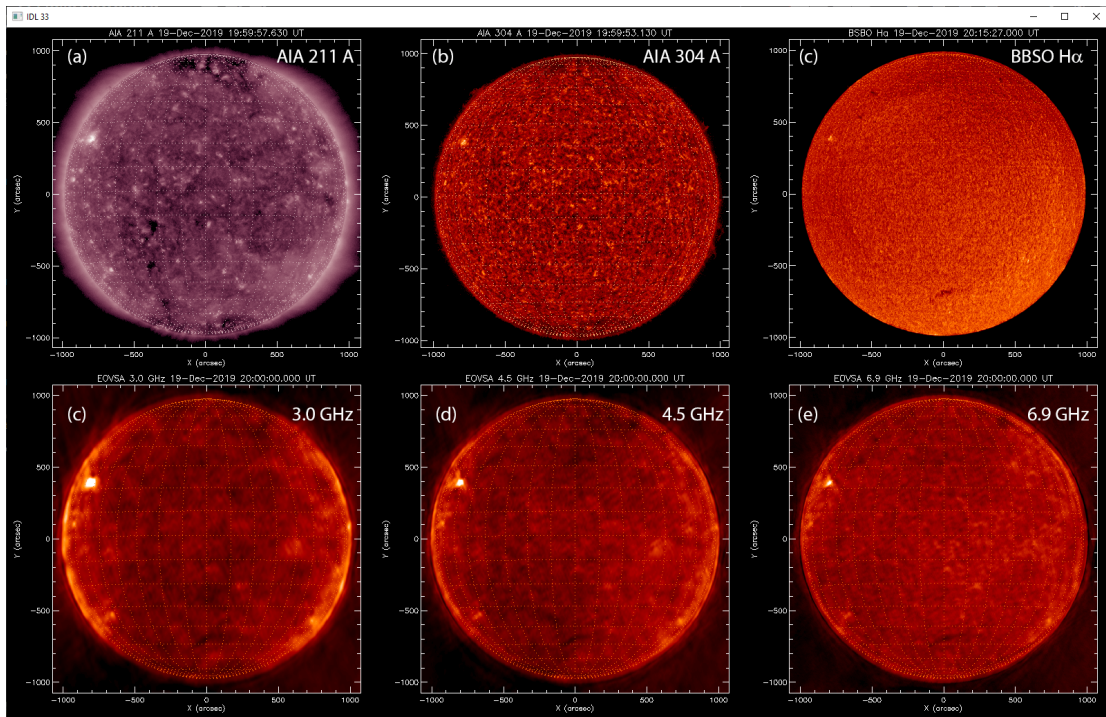


Fig.1: EOVSVA solar radio images from 2019 Dec 19 at three frequency bands showing a range of features.. (a) AIA 211 A image. (b) AIA 304 A image. (c) H α image from Big Bear Solar Observatory (BBSO). (d-f) EOVSVA microwave images centered at observing frequencies 3.0, 4.5, and 6.9 GHz. Figure 1d-f show images (frequencies increasing from left to right) from EOVSVA, displaying limb brightening from the diffuse corona, polar coronal hole darkening, multiple compact sources, and dark absorption features due to filament channels. Just above each radio image are extreme ultraviolet (EUV) comparison images showing similar features from the AIA instrument on the Solar Dynamics Observatory (SDO), and an H α image from NJIT's Big Bear Solar Observatory.

2. COMPARISON WITH PREVIOUS WORK

2.1 Solar Full Disk Imaging Examples from History

The earliest attempt to define the brightness temperature profile of the quiet Sun was that by Christiansen & Warburton (1955) at wavelength of 21 cm (2.8 GHz). The result shown in Figure 2.1, based on multiple one-dimensional scans of the Sun during the solar minimum period 1952-1954, shows remarkably well the main features of equatorial limb brightening and polar darkening.

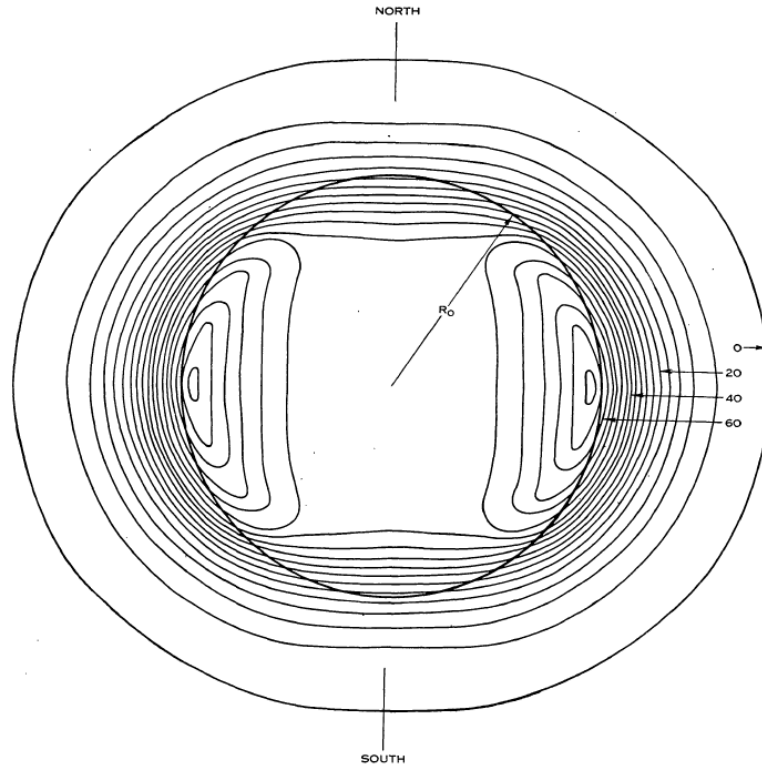


Fig. 2.1: *Solar disk brightness profile based on one-dimensional scans by Christiansen & Warburton (1955).*

Despite this early success, imaging the full disk of the Sun has been surprisingly rare for several reasons: (1) Full-disk scans by single antennas lack the spatial resolution needed except at high frequencies where limb brightening and polar hole darkening is greatly reduced. (2) Interferometric imaging of the Sun is difficult due to this large size, since without short antenna spacings the large-scale brightness features are lost. (3) When arrays such as the Jansky Very Large Array are used, the individual dishes are too large and restrict the field of view, requiring mosaicing techniques.

Figure 2.2 shows a rare success in multifrequency full disk imaging, from Saint-Hilaire et al. (2011) using the Allen Telescope Array. Unfortunately, this all-day synthesis observation was done only once, on 2010 Mar 21, and the ATA resolution was relatively poor ($4.5''/\nu_{\text{GHz}}$). Nevertheless, the frequency-dependent limb brightening is clear.

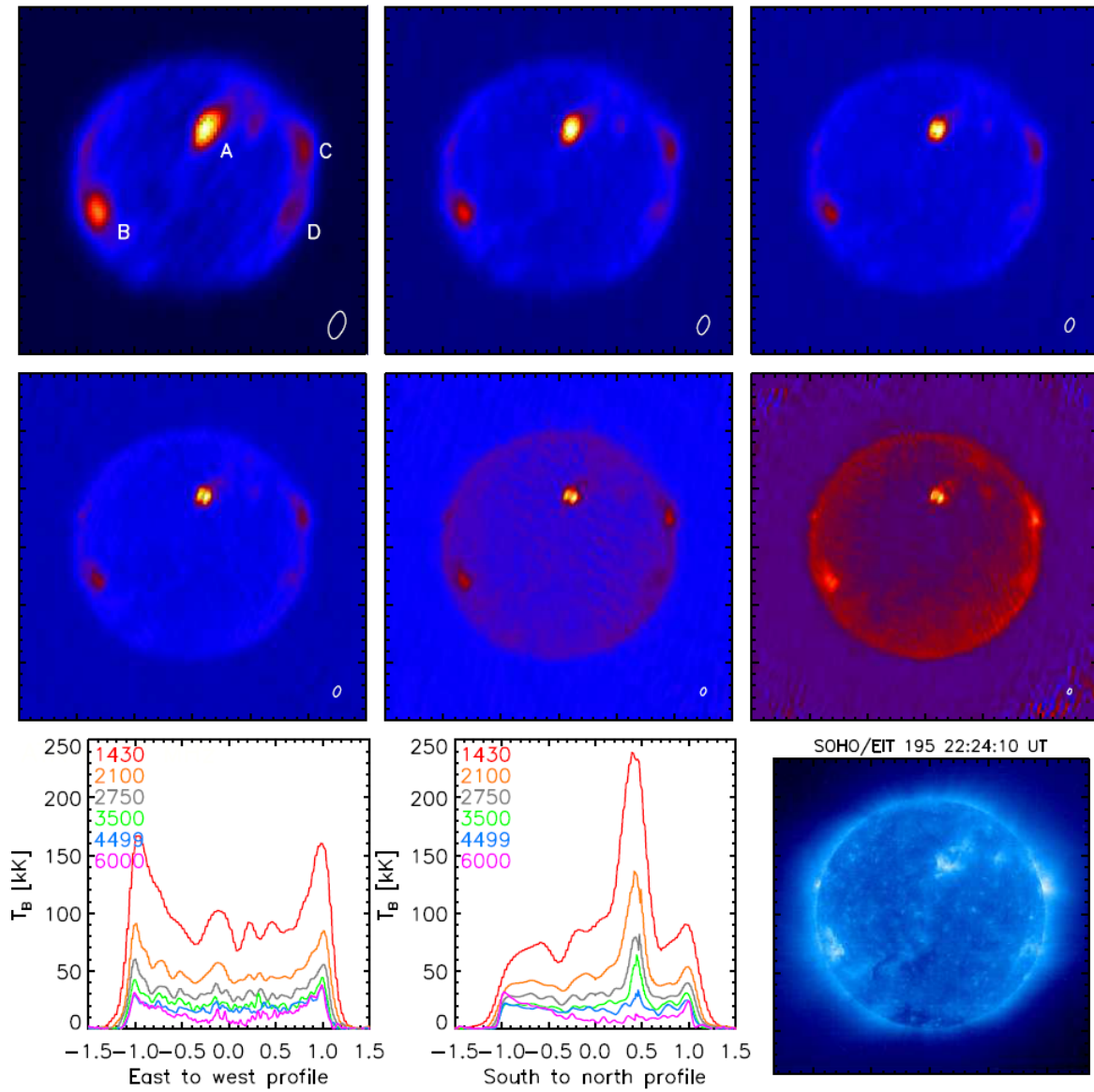


Fig. 2.2: Brightness temperature maps at 1430, 2.1, 2.75, 3.5, 4.5, and 6 GHz. An EUV image is shown at lower-right for comparison. Equatorial and polar profiles at multiple frequencies are shown in the bottom left and center. From Saint-Hilaire *et al.* (2011).

2.2 The EOVS A Breakthrough

With the imaging and calibration techniques described in Section 5 of this poster, EOVS A is now producing **DAILY** multi-frequency images of the quiet Sun with a resolution of about $0.6''/\nu_{\text{GHz}}$, 7.5 times better resolution than the ATA images, and at a wider range of frequencies. Figure 2.3 shows an example of the 6 frequency bands, for an extremely quiet day in deep solar minimum. There are no spotted regions on the disk--the compact sources are small magnetic bipolar regions with no sunspots.

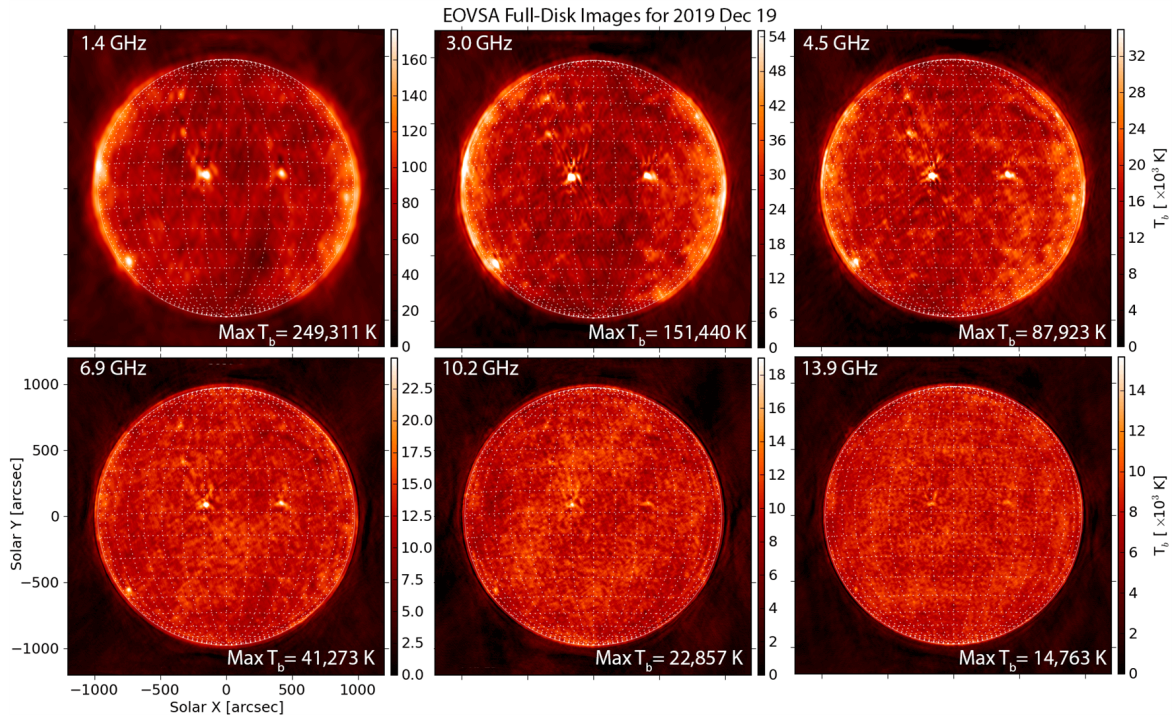
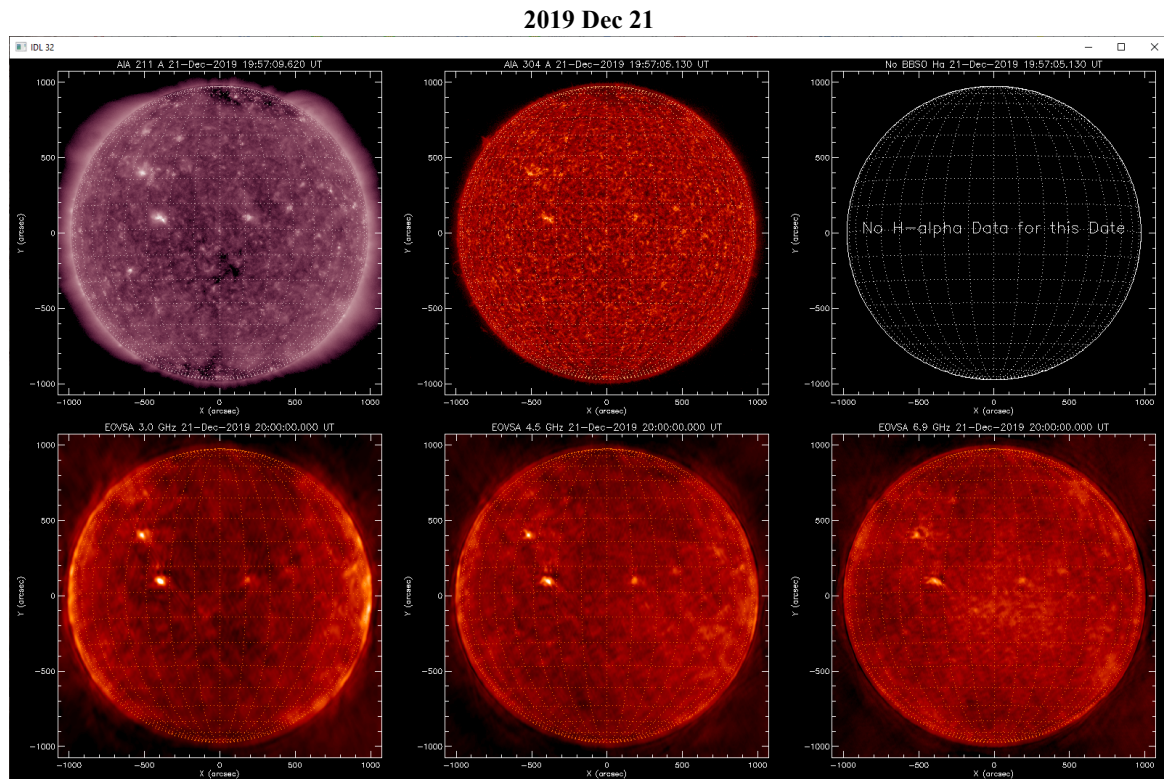


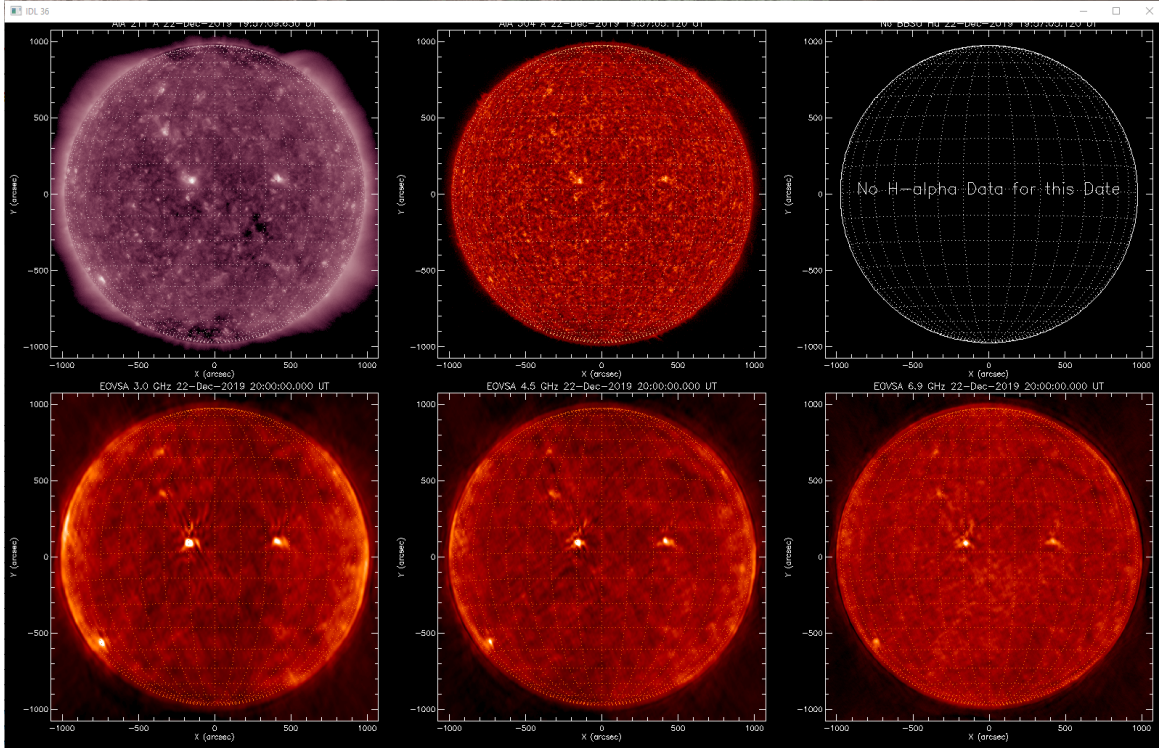
Fig. 2.3: Example of the daily output of the EOVSA full-disk pipeline, which automatically creates images in these 6 frequency bands. Each panel gives the maximum brightness temperature for that image, while the color bar shows the color scale in units of 1000 K.

The figures below show several consecutive days in late December 2019, to show the variation of the Sun as new regions appear and rotate across the disk. Unfortunately, bad weather at BBSO prevented H α images from being taken on these dates. You can also watch an animated video of the 4.5 GHz images.

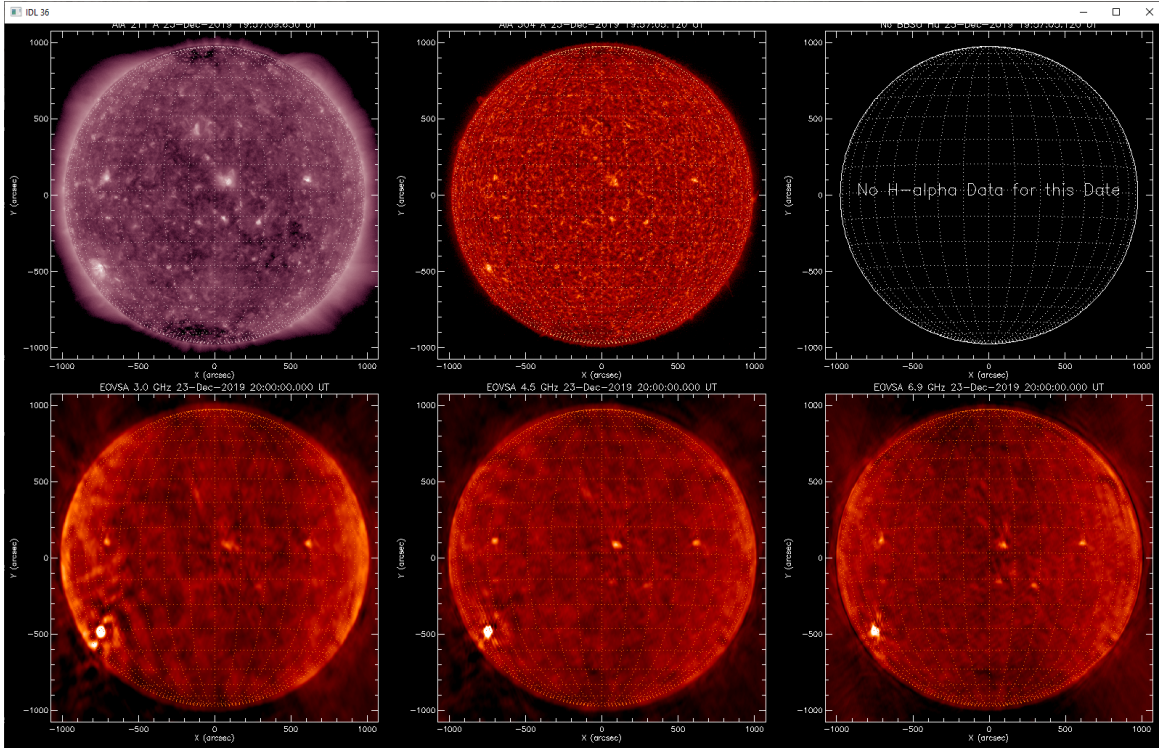
[VIDEO] <https://www.youtube.com/embed/qIu92PGZJEK?feature=oembed&fs=1&modestbranding=1&rel=0&showinfo=0>



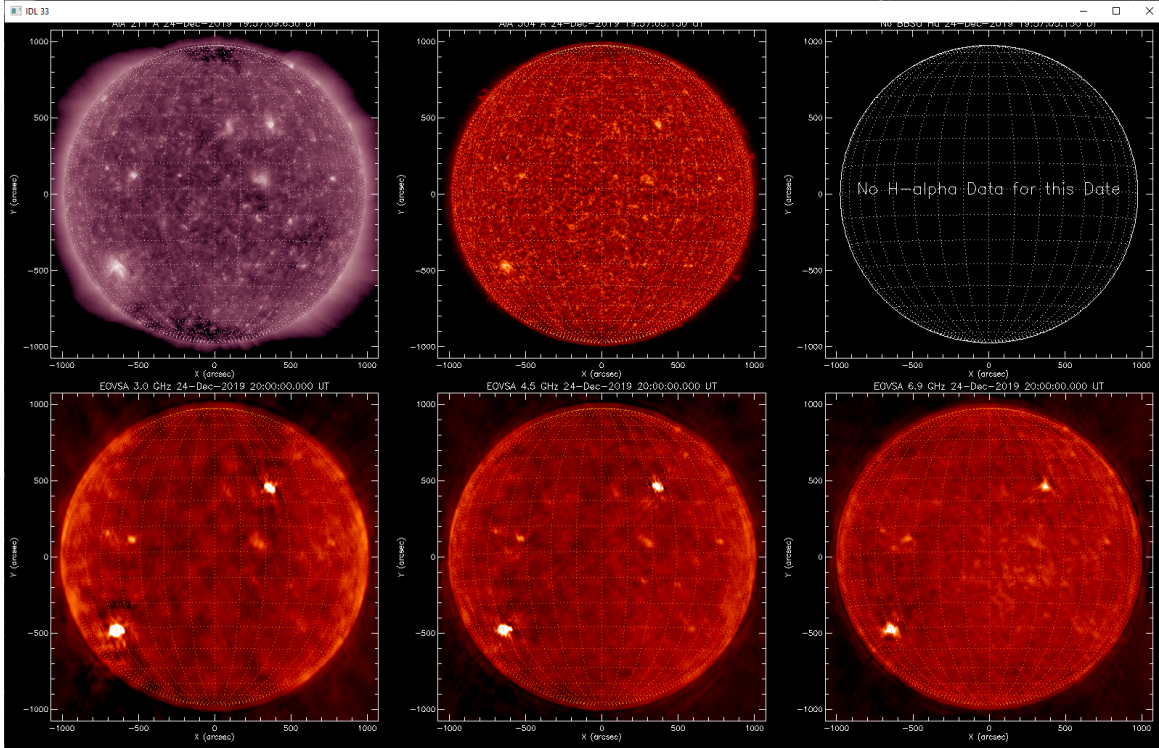
2019 Dec 22



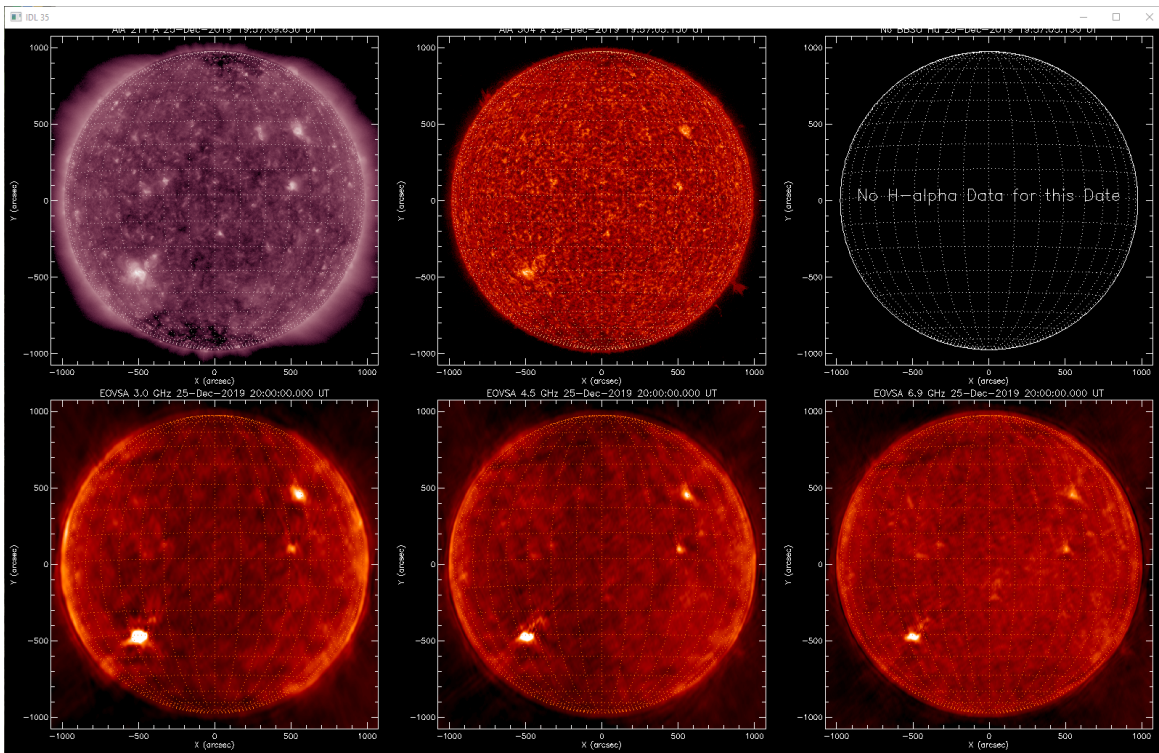
2019 Dec 23



2019 Dec 24



2019 Dec 25



3. LIMB BRIGHTENING AND CORONAL HOLE DARKENING

3.1 Cross-sectional Profiles

The equatorial regions of the radio images show clear limb brightening, where the edges of the Sun are brighter than the disk center, as is well known since first reported by Christiansen & Warburton (1955), and further improved upon by several authors including Saint-Hilaire et al. (2011).

The EOVSAs show not only the general effect, but clear correspondence with the detailed structure, which is easier to see when the radio images are compared with a degraded resolution AIA image, as in Figure 3.1. Contours from the AIA image are overlaid on the EOVSAs in the lower right.

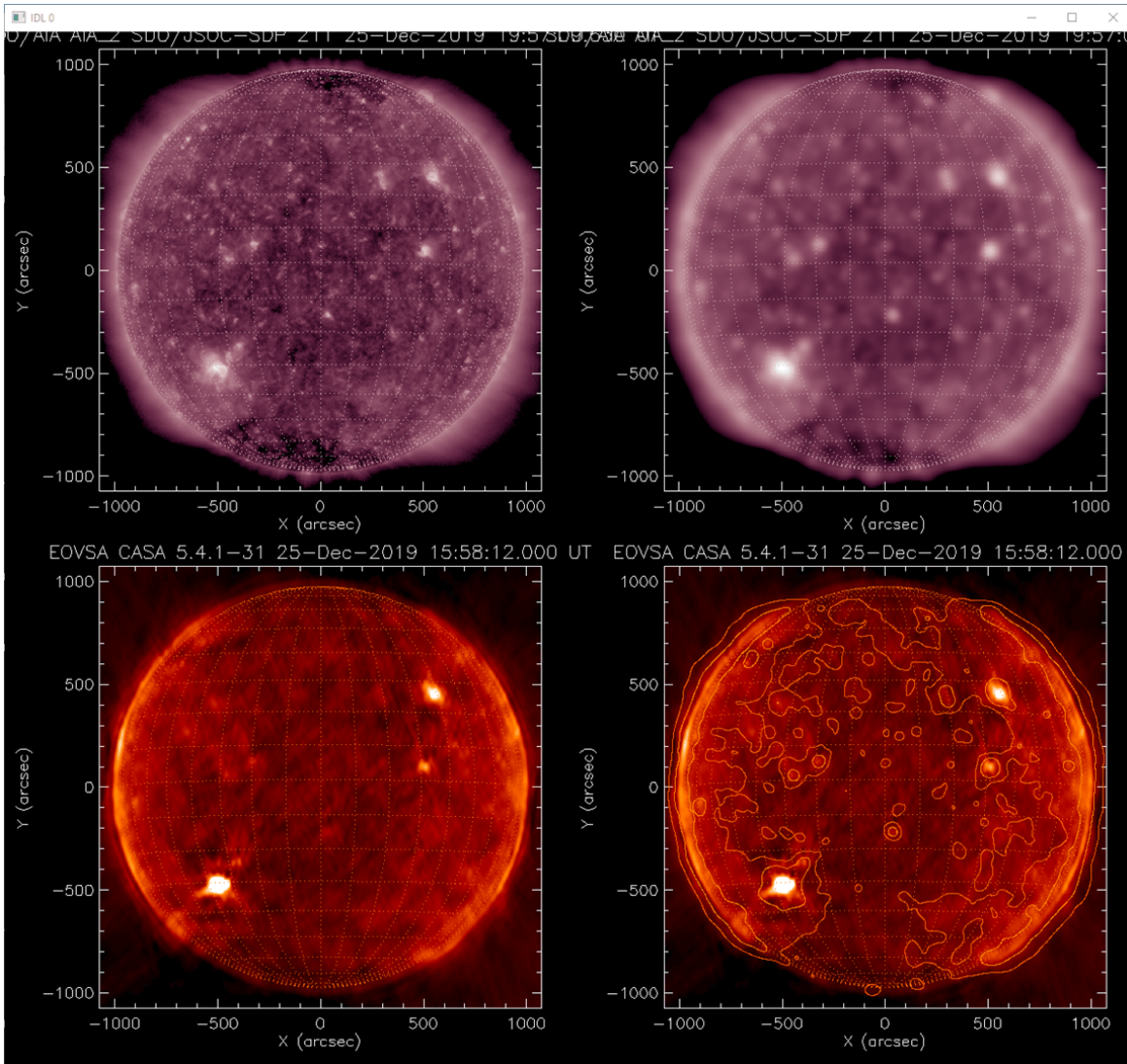


Fig. 3.1: A comparison of coronal limb brightening for images taken on 2019 Dec. 25. The AIA image in upper left is degraded in resolution, upper right, and then contours from the degraded image are overplotted on the EOVSAs 3.0 GHz map in lower right.

Because the detailed shape of the limb brightening varies from day to day, it is best to average over many days to get an average profile. Figure 3.2 shows the average limb brightening and polar darkening profiles at our 6 frequency bands averaged over 63-70 days (precise duration varies with frequency). The result on the left shows a clear equatorial limb spike that decreases in brightness with frequency, while for the polar profiles (right panel) the disk is much flatter and lacks a clear limb spike. Note that the disk is considerably larger than the photospheric radius, shown by the dashed vertical lines.

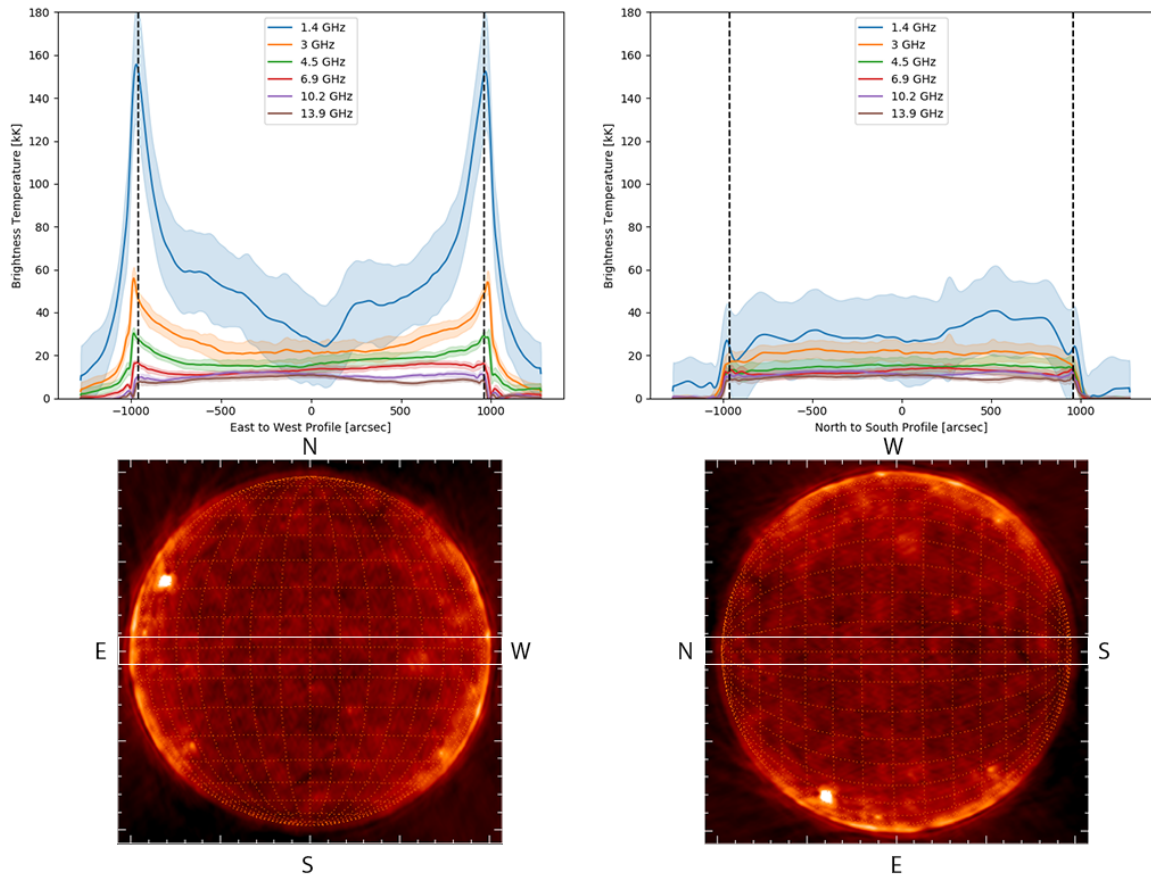


Fig. 3.2: Upper row, brightness temperature profiles in the equatorial direction (left) and polar direction (right) averaged over many images taken over more than 60 days in 2019 Oct-Dec.. The light-colored bands represent ± 1 standard deviation. The lower panel shows one example for illustration (rotated by 90 degrees in the lower left panel).

Figure 3.3 shows a direct quantitative comparison between our multi-frequency results and those for a single date by Saint-Hilaire et al. (2011), as shown also in Figure 2.2. The limb spike amplitudes are remarkably similar, but the 7.5 times higher spatial resolution for EOVSVA is evident.

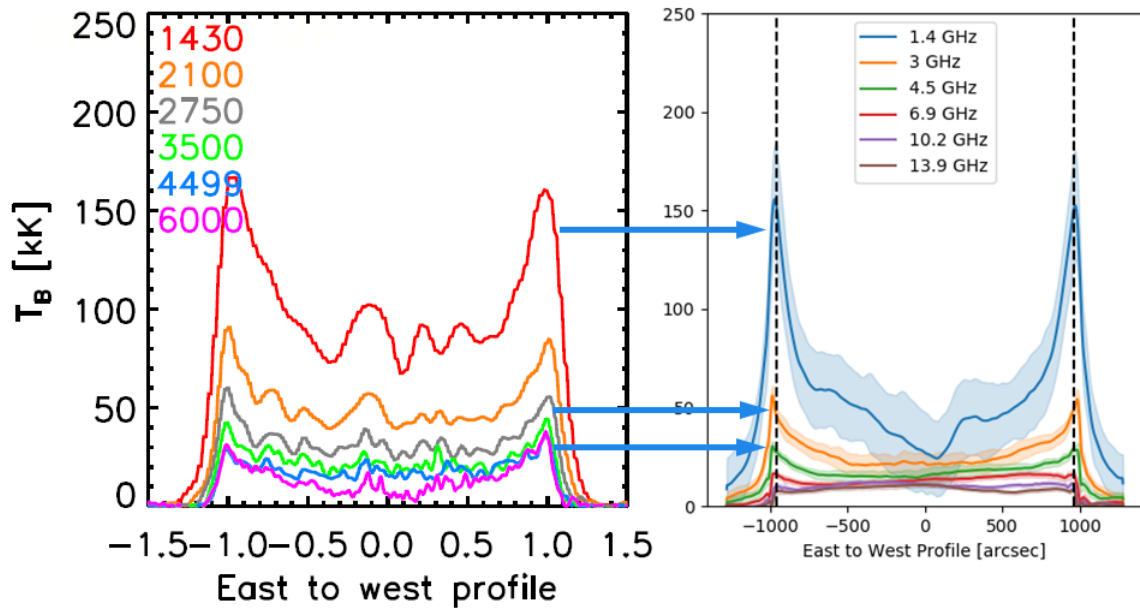


Fig. 3.3: Quantitative comparison of these averaged EOVSVA results (right panel) with the Saint-Hilaire et al. (2011) results for a single day in 2010. The limb spike amplitudes are remarkably similar at corresponding frequencies (indicated by the blue arrows).

3.2 Azimuthal Profiles

It is interesting to see the position-angle dependence of the limb brightening, which reflects important differences in the structure of the solar atmosphere in the regions of the closed corona at low latitudes and the open corona at the poles. Figure 3.4 shows this limb profile and its standard deviation for all 6 frequency bands for position angles in steps of 5 degrees from north toward east. Not surprisingly, the two limbs are essentially identical, as are the two poles. The limb brightening is nearly constant from latitudes -60 to 60 (position angles 30-150 and 210-330).

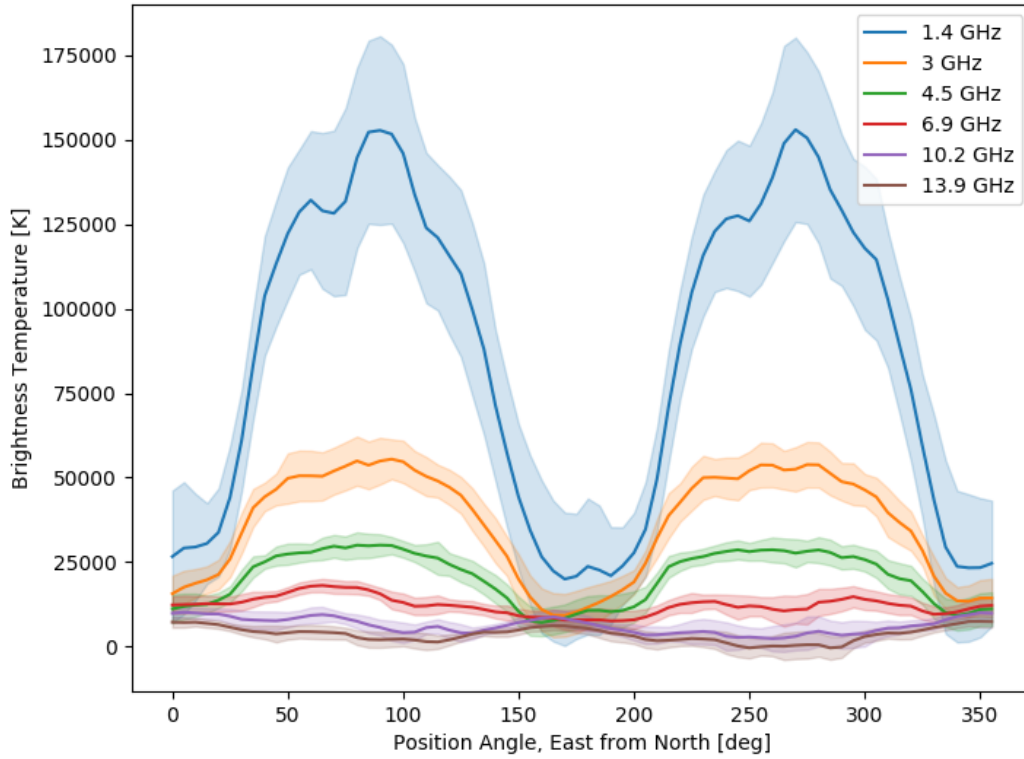


Fig. 3.4: Azimuthal brightness temperature profile at each of 6 frequencies averaged over more than 60 days in 2019 Oct-Dec.. The light-colored bands represent ± 1 standard deviation.

Figure 3.5 illustrates the day-to-day variation in these azimuthal profiles for the 3 lowest frequencies.

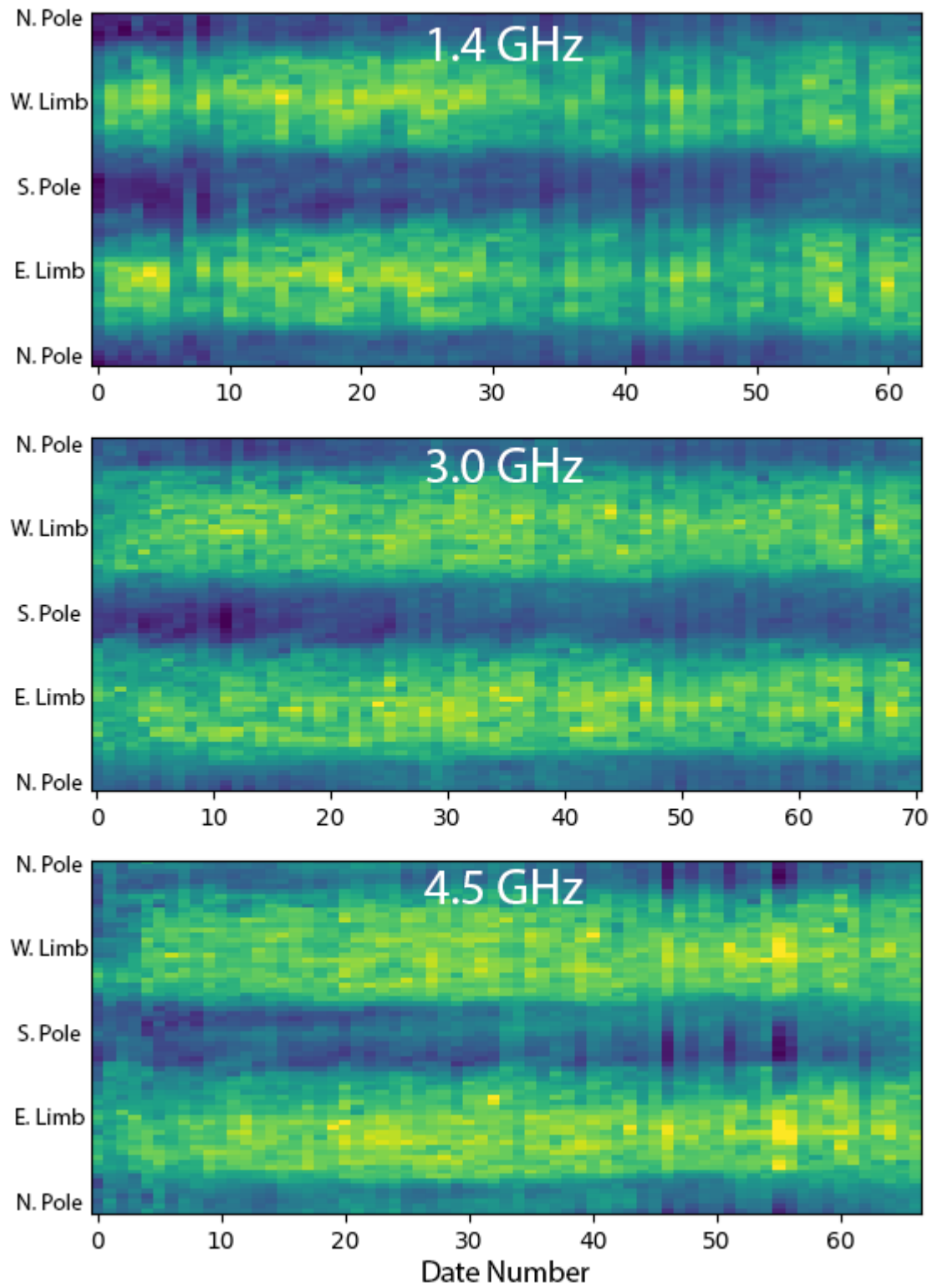


Fig. 3.5: Azimuthal profiles vs. time for more than 60 days in Oct.-Dec. 2019. The color scale shows the brightness temperature (scaled separately in each panel). The vertical direction is azimuth, with the poles and equatorial limbs labeled.

4. QUANTITATIVE MEASUREMENT OF PHYSICAL PARAMETERS

4.1 Brightness Temperature vs. Temperature

In radio astronomy, we make use of the Rayleigh-Jeans regime ($h\nu \ll kT$) to write the black-body source function in terms of temperature. Thus, in the radio regime brightness, or intensity, can be expressed conveniently as a brightness temperature. However, a source only reaches this brightness if it is optically thick. If not, its brightness temperature is lower, $T_b = \tau T$ where $\tau < 1$ is the optical depth. The solar corona presents that case of an optically thin source, which is seen against a background chromosphere that is optically thick, but at a much lower temperature.

Following Saint-Hilaire et al. (2011), we simplify the situation to

$$T_b = T_{ch} + \tau T_{co}$$

where T_{ch} is the temperature of the background chromosphere, typically around 10,000 K, and T_{co} is the temperature of the corona, at least 1 MK.

4.2 Relating Measured Brightness Temperature to Column Emission Measure

When the magnetic field in the source is not too high (say below a few hundred gauss), the emission is entirely due to the free-free (Bremsstrahlung) mechanism. Again following Saint-Hilaire et al. (2011), the free-free optical depth is given by

$$\tau = \zeta \nu^{-2} \frac{EM}{T^{3/2}},$$

where EM is the column emission measure in units of cm^{-5} , ν is the observing frequency, T is the coronal temperature, and ζ is a slowly varying function of T and ν given approximately by (Dulk, 1985):

$$\zeta(T/\nu) = 9.786 \times 10^{-3} \ln(4.7 \times 10^{10} T/\nu).$$

Since the coronal temperature is typically within about 1/2 dex of 10^6 K, we will write this in units of millions of K, and compute η -maps defined as

$$\eta = \frac{EM}{\sqrt{T_6}} = 1000 \nu^2 \frac{T_b(\nu) - T_{ch}}{\zeta}.$$

What this amounts to is subtracting a constant temperature from each map, scaling the resulting brightness temperature by the observing-frequency-squared, and then applying the constant scale factor ζ to get column emission measure. If the so-scaled brightness at each frequency is the same in a given brightness feature, then that feature is consistent with being due to free-free optically-thin emission from a hot corona.

4.3 Spotless Bipolar Plage Regions

Figure 4.1 is a tutorial on how the emission measure is determined from the EOVSAs multi-frequency images. The background image shows the selection of a square region 40 x 40 pixels. The row of extracted images for each frequency is shown. A 2d-Gaussian is fit to each image (the fit failed for 1.4 GHz in this example), and the peak brightness temperature from each fit is determined as well as the average background level. In the plot on the upper left, the green points show the measured background level. The red points show the total brightness temperature after subtracting a constant $T_{ch} = 10,000$ K. If these values are due to optically-thin free-free emission, T_b should fall as ν^{-2} . The plot in the upper-right then shows the corresponding values of column emission measure. The values for frequencies 3.0-10.2 GHz are nearly constant at 10^{28} cm^{-5} , strongly suggesting that this is a good measurement. At the lowest frequency the deduced EM is very low, but this is due to the bad 2d-Gaussian fit. At the highest frequency the value is also low, because it depends strongly on the value chosen for T_{ch} . Finally, rather than fitting a 2d-Gaussian and getting only a single EM for this selected plage region, we can simply perform the calculation for every pixel, which yields the EM maps in the bottom row. These are scaled to the same EM range, $10^{26} - 10^{28} \text{ cm}^{-5}$.

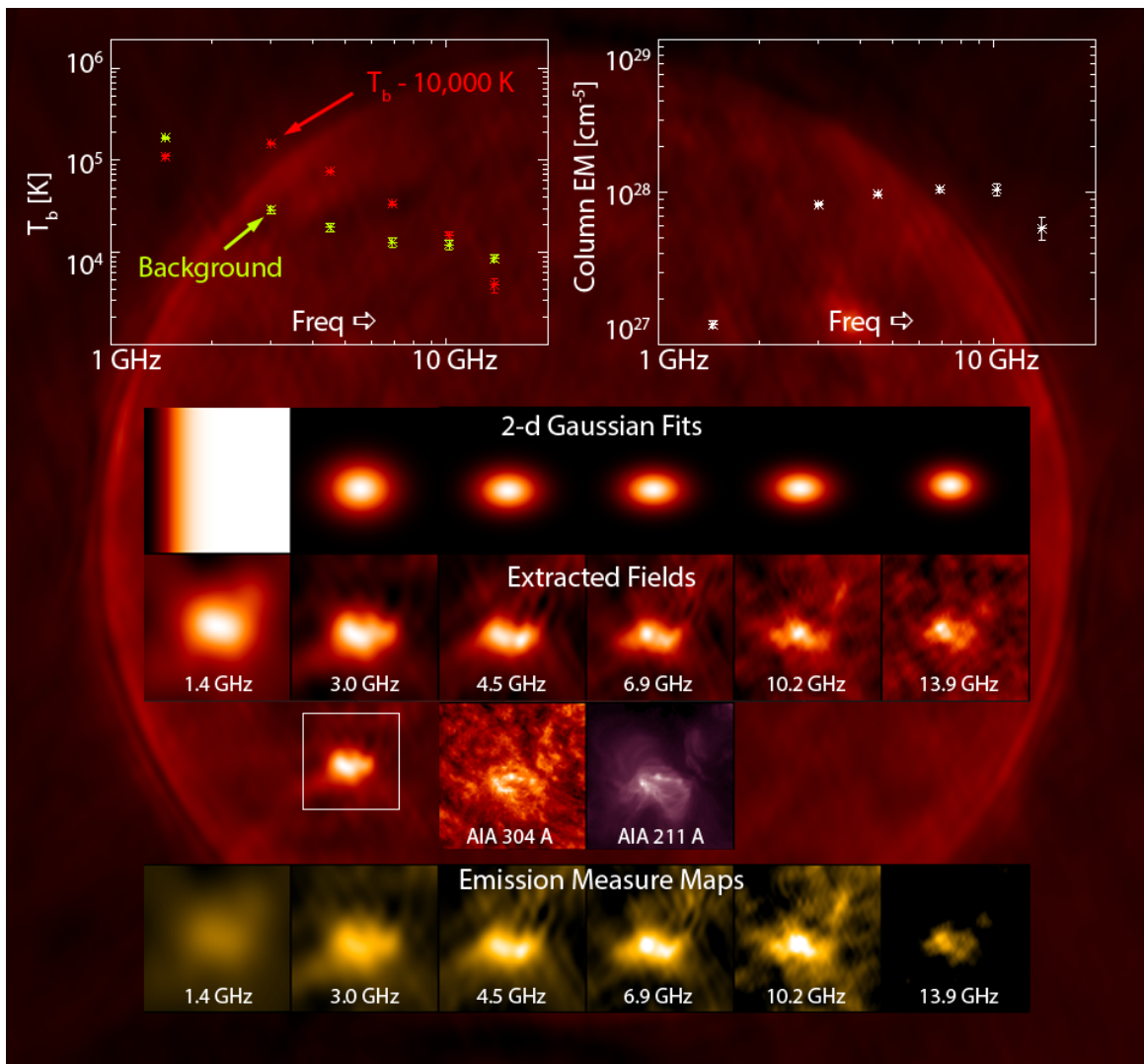


Fig. 4.1: Tutorial on how to calculate EM from EOVS multi-frequency images. See above text for details. This example is from 2019 Dec. 25.

In fact, it is not necessary to calculate EM only in small selected regions, but rather the entire images can be used to map full-disk EM maps! Figure 4.2 shows EM maps calculated for 1.4, 3, 4.5, 6.9, and 10.2 GHz. Each of these maps is calculating the same EM, hence they should look identical. Except for resolution, and increasing noise at higher frequencies, they indeed agree remarkably well. Again, the highest frequency image is compromised due to the choice of $T_{ch} = 10,000$ K being close to the disk level, leaving almost no free-free emission. The bottom-right panel is an average over the 3.0, 4.5, and 6.9 GHz maps. It is remarkable that the filament channel in the north becomes exceptionally clear in this average EM map.

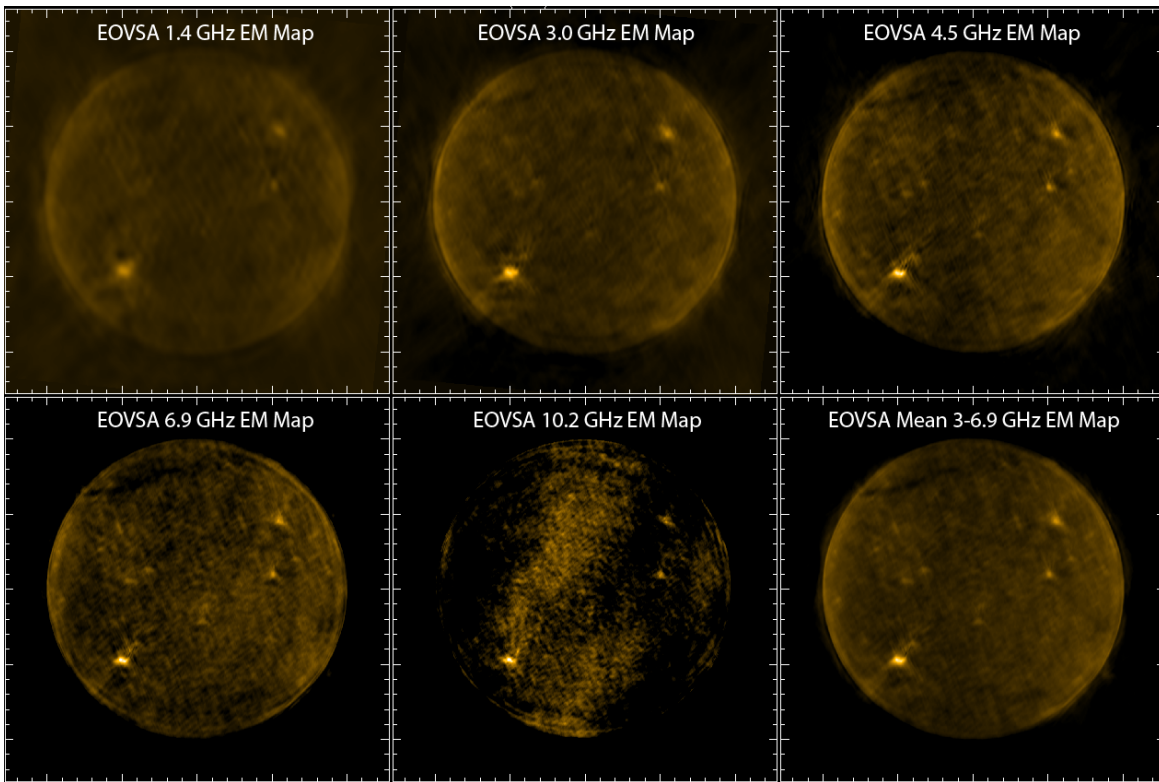


Fig. 4.2: Full-disk EM maps for 2019 Dec. 25 at 5 frequencies, all scaled to the same EM range, and an average map (lower-right) based on the three images in the top row. Note the clear filament channel in the north in this average map.

Figure 4.3 gives a more quantitative comparison for a diagonal cut through the EM maps that crosses the two brightest plage regions. Despite some fluctuations, the overall EM agrees fairly well with that from the average map (the black curve).

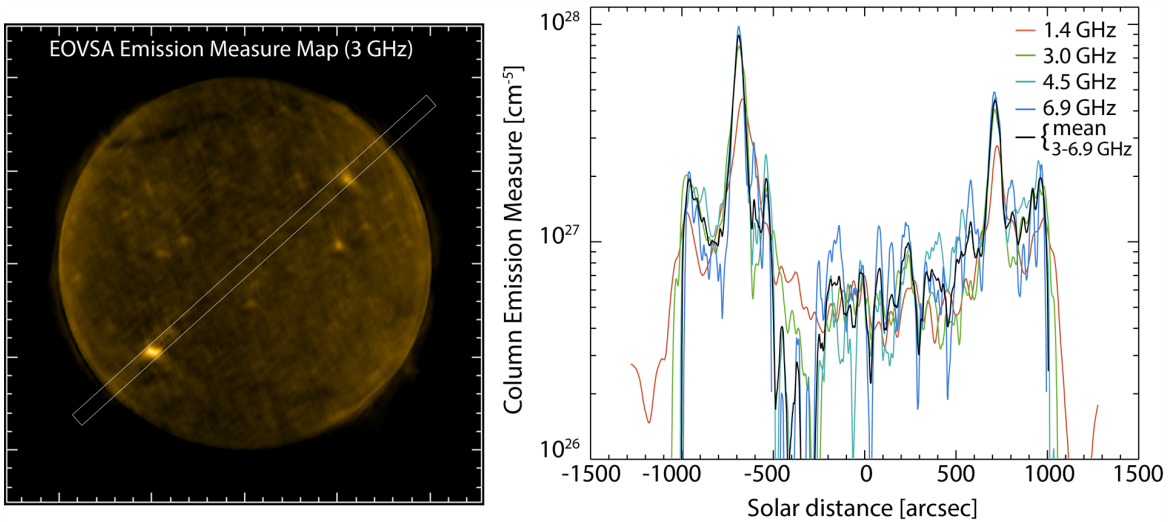


Fig. 4.3: Quantitative comparison along the cut shown in the left-hand panel. The overall limb brightening pattern is evident, along with the spike in EM over the two plage regions.

Figure 4.4 gives a quantitative comparison with emission measure determined from AIA DEM analysis (see the AIA DEM tutorial (https://www.lmsal.com/~cheung/AIA/tutorial_dem/)). For this comparison, the DEM maps have been summed to give a total column emission measure, and the result degraded in resolution for a more direct comparison with EOVSAs. Feature-for-feature, the two compare extremely well although the EOVSAs disk EM is higher. Recall that the EM in AIA is from ion emission while that from EOVSAs is from electrons.

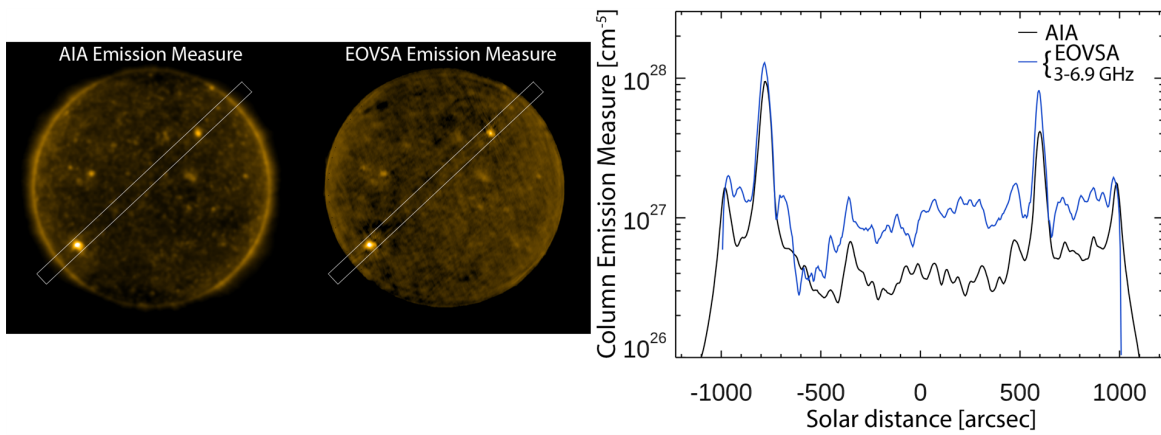


Fig. 4.4: *Quantitative comparison between AIA emission measure and EOVS. The two images (shown with a square-root color table) are shown on the left, and a comparison along the cut shown is on the right.*

4.4 Spotted Regions

Although we are at solar minimum, there are occasionally regions showing small and weak sunspots. In such regions a new emission mechanism, gyroresonance emission, becomes important in small regions over the spots. A sequence of emission measure spectra for Dec. 23-25 (Figure 4.5) illustrates this extra emission (about a factor of 2 at 4.5 GHz). Note that the EM measurement has no meaning in the small areas where gyroresonance emission is playing a role.

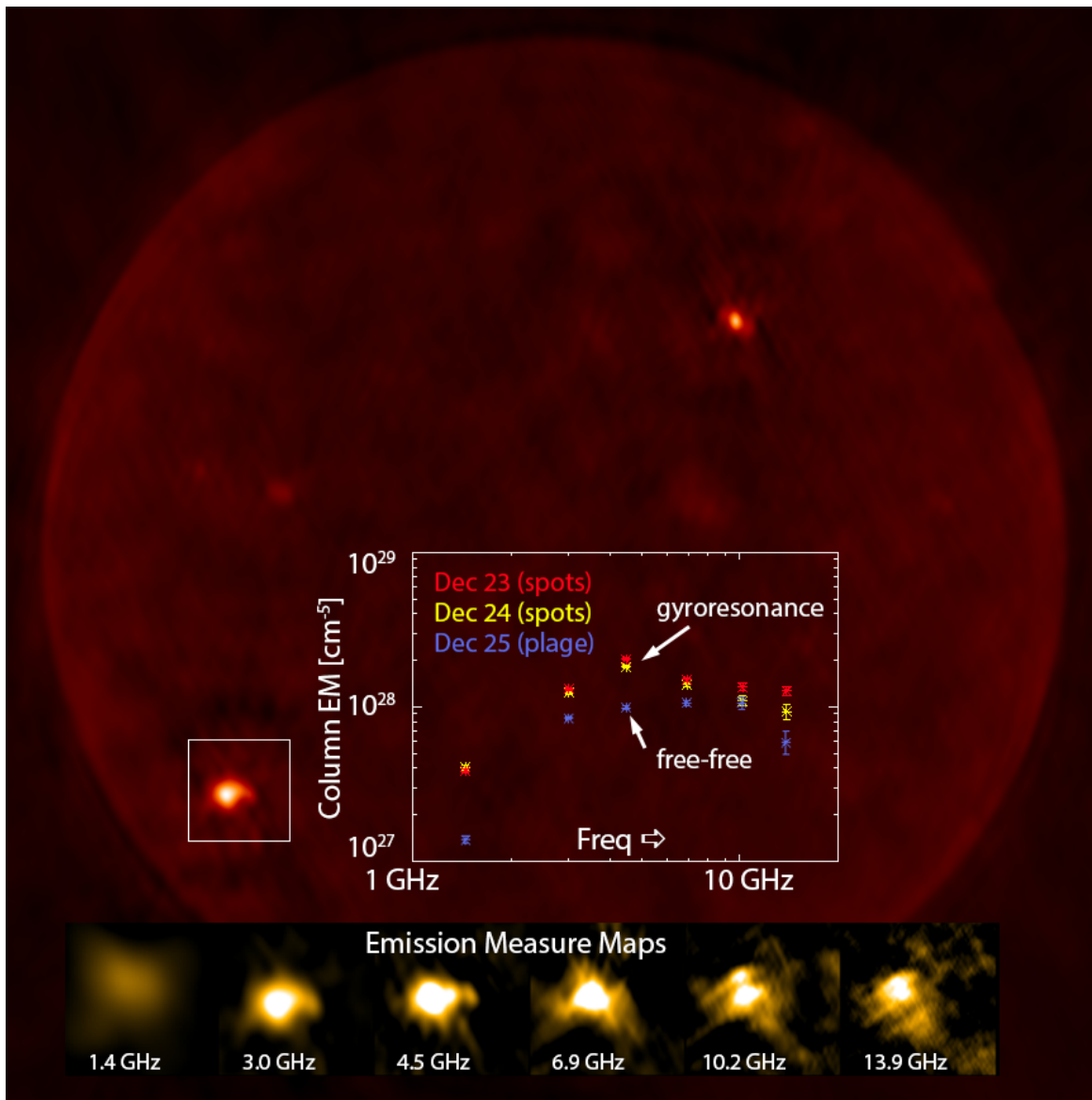


Fig.4.5: The emission measure spectra for 2019 Dec. 23-25. The selected region had spots on Dec. 23 and 24, which caused the EM spectrum to have a peak near 4.5 GHz and be elevated at all frequencies. By Dec. 25, the EM spectrum again became flat, indicating optically-thin free-free emission.

This effect can become extreme when large spots are on the disk, as in the example in Figure 4.6, taken 2019 May 06. Now the brightness temperature is completely optically thick due to gyroresonance emission, reaching ~ 2 MK, and the EM spectrum is very much NOT constant. Although it should still be possible to measure EM elsewhere in the images, the limited dynamic range coupled with the very bright source implies that getting EM maps with EOVSAs can only be done reliably at solar minimum. We need an array with EOVSAs's capabilities, but with many more antennas.

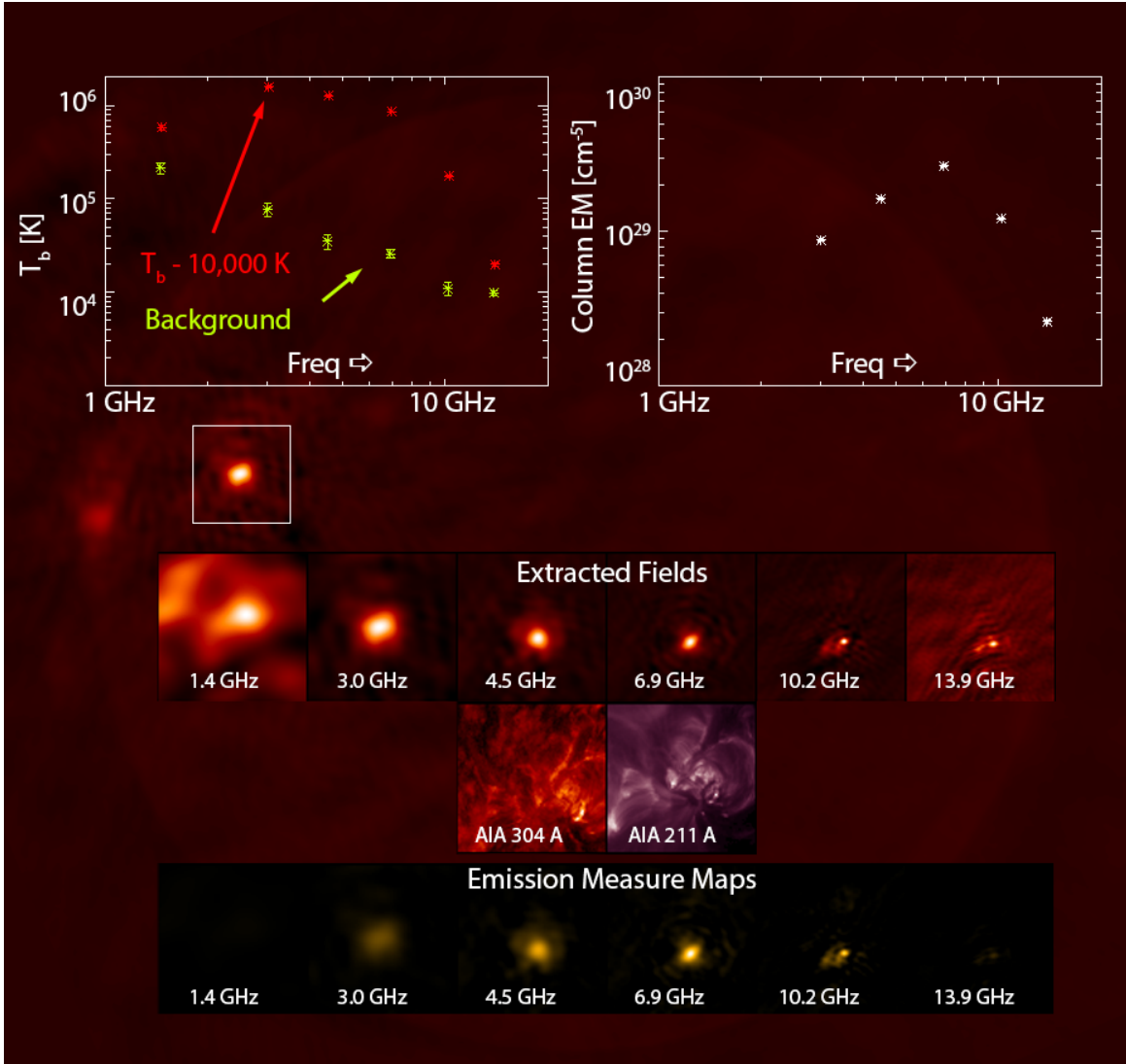


Fig. 4.6: The emission measure spectrum for 2019 May 06, when a large sunspot was on the disk. Such a strong source makes EM measurements very difficult with EOVSAs during solar minimum.

5. CALIBRATION AND FULL DISK IMAGING PIPELINE

5.1 Imaging with 13 Antennas

Making these full-disk images is not easy with only 13 antennas, but we are greatly helped by a technique called frequency-synthesis, and by making the image over an entire 8-hour day while the Earth rotates.

Radio arrays make measurements in spatial Fourier space (called the uv plane), which are then Fourier inverted to form an image of the sky plane. The more fully an array samples the uv plane (i.e. the more antennas and the better the spacing of the antennas) the more the images improve.

We can illustrate this uv coverage for EOVSVA (using the coverage for 2019 Dec 19). Figure 5.1 shows the time coverage over the day, including gaps for calibrations. The color scale shows the amplitude of the signal vs. frequency and time over a bit less than 8 hours. The fringe patterns in the data represent the spatial structure of the solar disk.

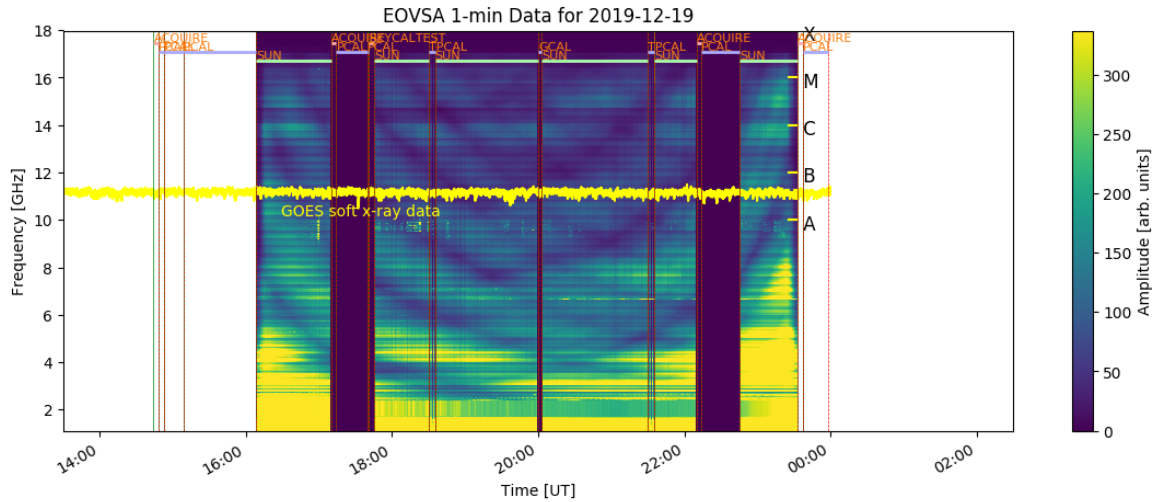


Fig. 5.1: Daily baseline amplitude plot for 2019 Dec. 19 showing the time coverage on the Sun for that day, including gaps for calibrations. The yellow trace is the GOES 1-8 A soft X-ray plot, which is completely flat because of solar minimum conditions.

The uv coverage for this date is illustrated in Figure 5.2. The 13 antennas form 78 distinct baselines (pairs), which appear as points in the uv plots of Fig. 5.2. The location of the point for a given pair of antennas is a linear function of frequency, so when points are shown for 10 frequency bands, they form a line of 10 equally-spaced dots radiating from the center (Fig. 5.2a). Combining frequencies like this is called frequency synthesis. If we integrate over the entire day, the pattern rotates and changes scale, as shown in Fig. 5.2b. The same pattern for lower frequencies is shown in Fig. 5.2c. The difficulty of imaging the Sun is shown by Fig. 5.2d, where we plot the inner $1 \text{ k}\lambda$ of the uv plane and compare it to the scale of the disk of the Sun (black circle). This "hole" in the uv plane means that we do not sample very well the spatial scales of the $1/2$ degree disk.

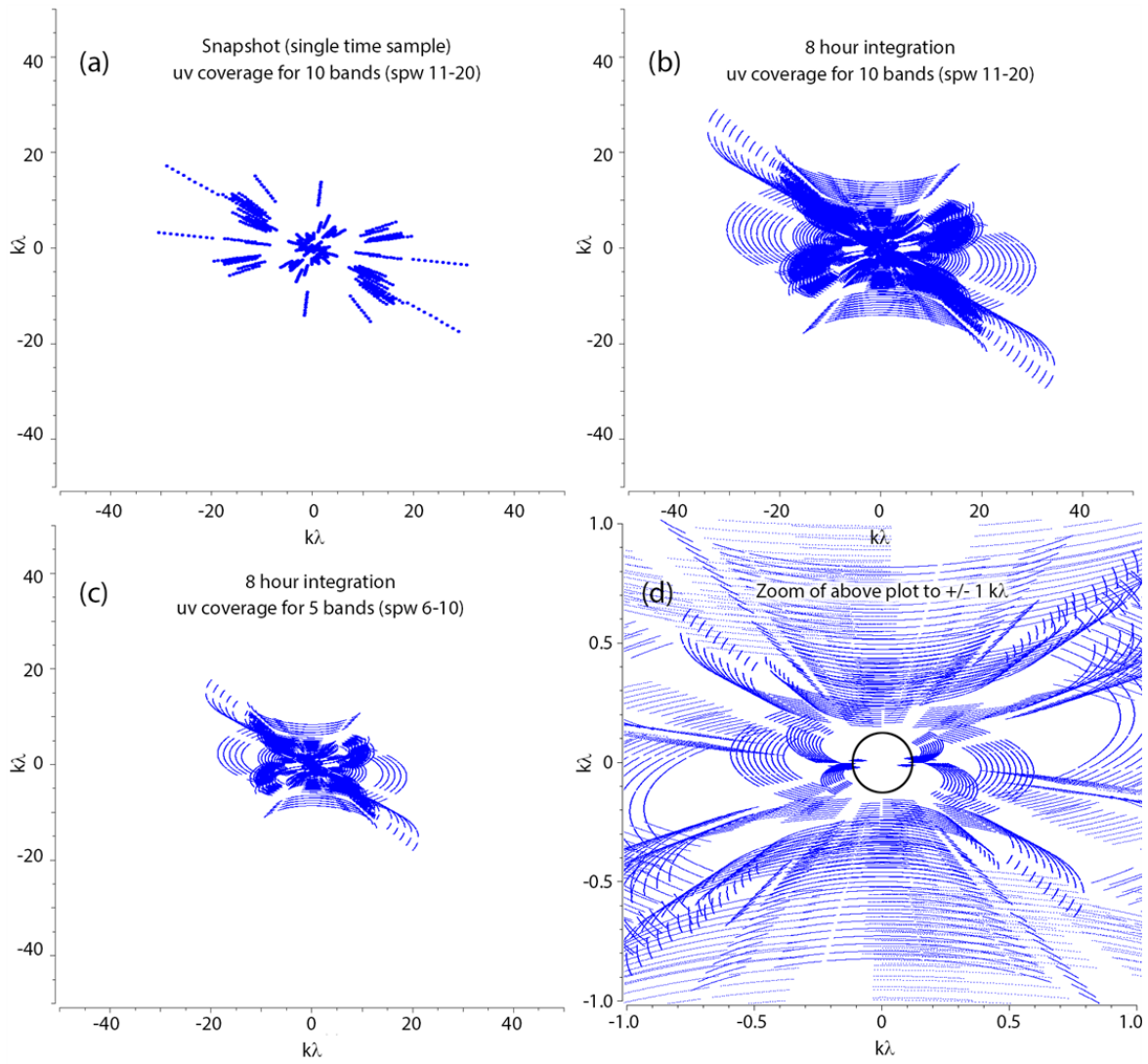


Fig. 5.2: Illustration of uv coverage of EOVSAs for 2019 Dec 19. (a) Coverage for 10 bands (spectral windows 11-20, with center frequency 4.5 GHz) at a single time around the middle of the day. (b) Coverage for the same frequencies as (a), for the entire day, include gaps for calibrations. (c) The same as in (b), but for 5 lower-frequency spectral windows (2-6), with center frequency 3.0 GHz. (d) A zoom of the points in (b) to the inner $1 k\lambda$. The black circle represents the extent of the disk of the Sun (0.5 degrees corresponds to ~ 114 wavelengths).

The Fourier transform of a disk is a J_0 Bessel function, or Airy pattern. Figure 5.3 shows the amplitude and phase of the disk signal as a function of uv distance in wavelengths, as seen in EOVSAs data in frequency bands 0, 4, 8, and 14. The main lobe of the disk and the "diffraction" rings are especially well seen in the higher spectral windows, and the phase shows the expected alternation between 0 and 180 degrees.

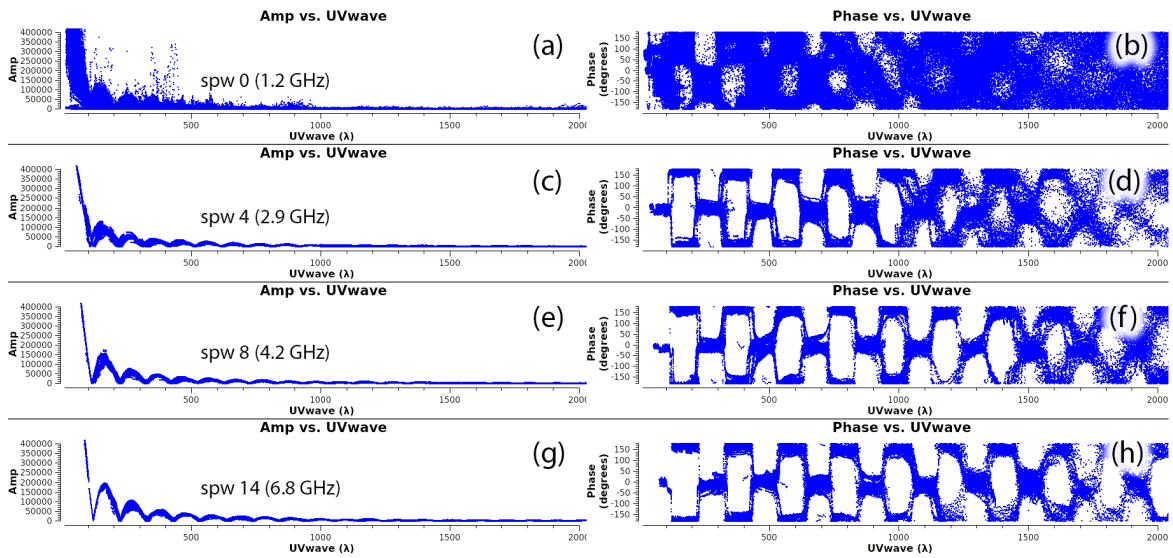


Fig. 5.3: Amplitude and phase vs. uv wavelength at four individual spectral windows, showing the dominance of the solar disk signal. The lowest frequency (spw 0) suffers from a lot of radio-frequency interference, not removed in this illustration. The data points start well down the primary lobe of the Airy pattern, due to the "hole" in the uv plane shown in Fig. 5.2d.

5.2 Modeling and Removing the Disk Signal

During solar minimum, by far most of the flux density is due to the quiet disk, yet as shown above this disk is not well measured. However, we can model the disk as a uniform and essentially unchanging circular disk throughout the solar minimum period, calculate the uv response to the disk, and simply subtract it from the data. One problem, though, is that the disk size changes with frequency because the height at which the solar atmosphere is optically thick grows higher with decreasing frequency. Subtracting the incorrect disk size will leave either a positive or negative ring depending on whether the disk is too small or too large. We have tried various methods to determine the disk size, including fitting the uv pattern shown in Fig. 5.3, but we find that the precision of such fits is not necessarily sufficient. For example, in Figure 5.4 we use simple trial and error by decreasing the disk size in steps of 1/2 percent until the residual negative ring is least noticeable.

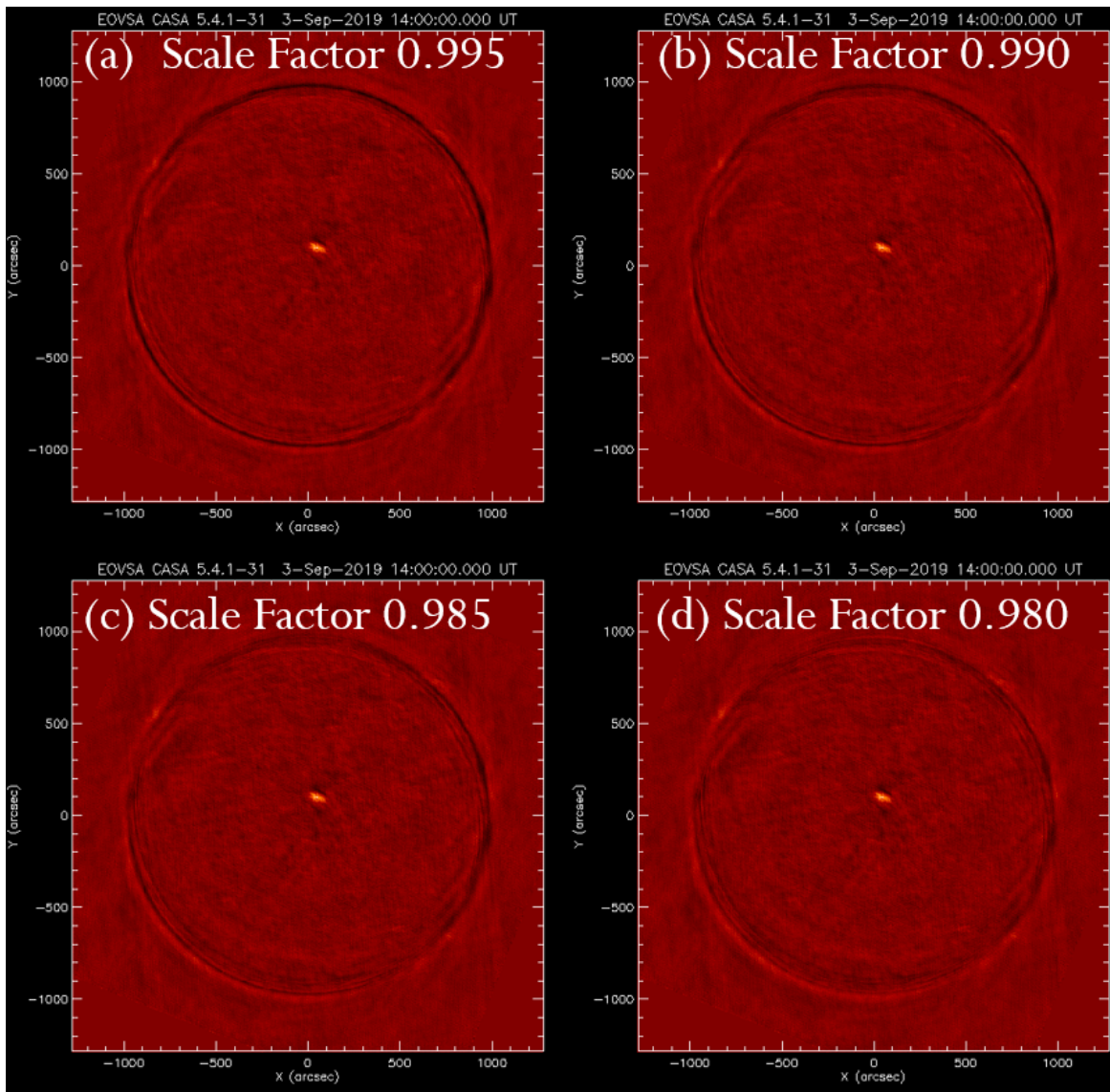


Fig. 5.4: Images made for 2019 Sep 03 by decreasing the disk size in 1/2 percent steps until the negative ring is least pronounced. The almost central spot in the images is an compact plage region that has nothing to do with the disk.

Ultimately, we determined the best disk size vs. frequency for a particular date, 2019 Sep 03, and simply scale the size for other dates according to the changing Earth-Sun distance. The flux density in the disk is also critically important. Again, for the particular date of 2019 Sep 03 the total integrated flux density tabulated by NOAA at 7 frequencies was fitted with a quadratic function to provide a flux density at each of our 50 bands. The combination of our adopted disk size vs. frequency and the measured total flux density provide the brightness temperature of the disk (and since this emission is optically thick, it also provides the temperature of the solar atmosphere vs. frequency). Once we have a good disk model, as shown in Figure 5.5, we can actually use that model to self calibrate the data! Individual antenna complex gains can be adjusted to correct for antenna-based errors to bring the corrected data closer to the model.

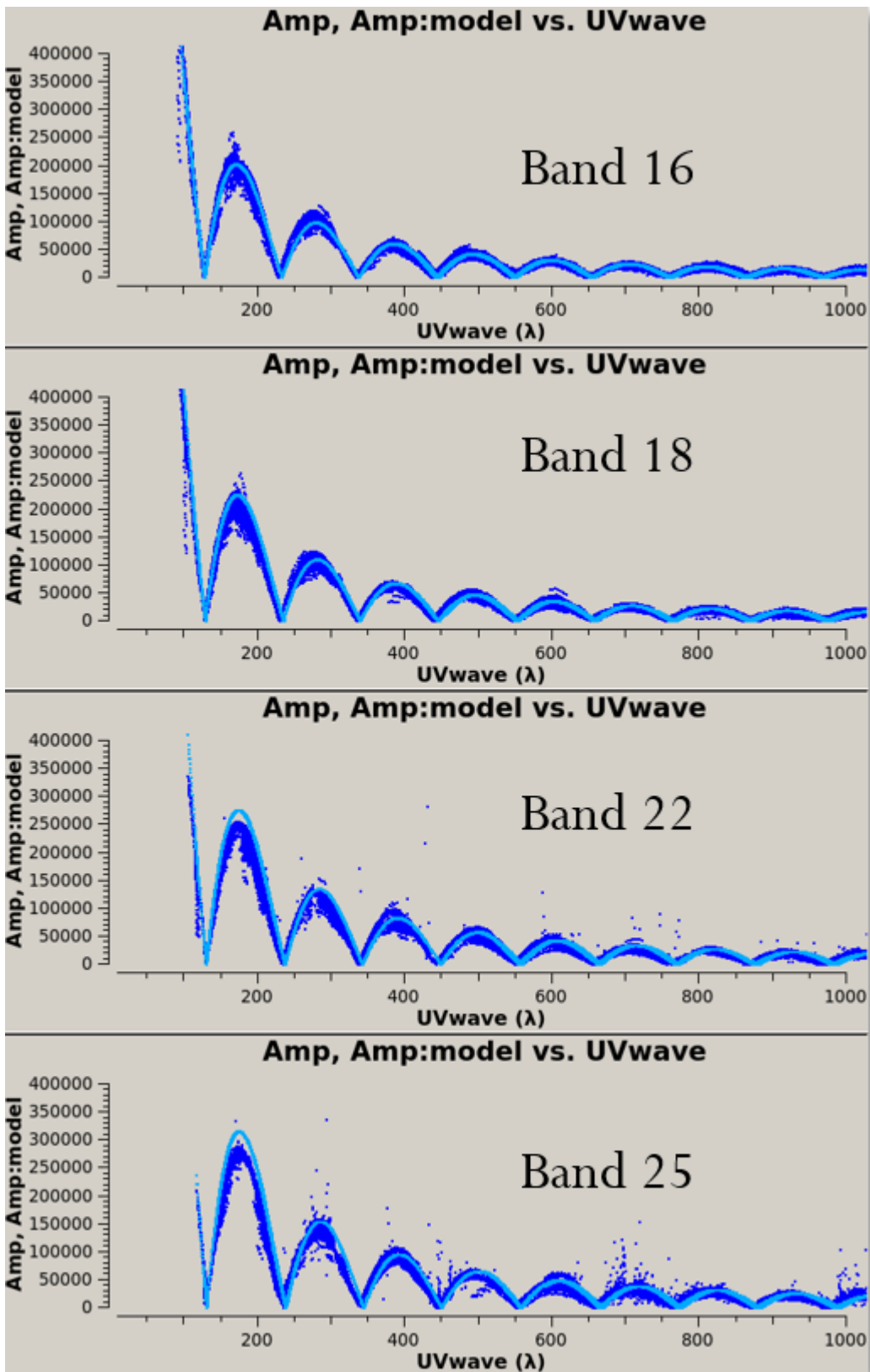


Fig. 5.5: Observed amplitude vs. baseline length (blue points), compared with the adopted disk model (cyan curve). Not only the shape, but also the amplitude pattern is uniquely determined by the disk model.

Once the data are self-calibrated to the disk model, the disk is subtracted. The residual image still has all of the other features of the solar atmosphere, such as plage or spot regions, limb brightening, filaments and prominences. The residual data are now processed through the normal image deconvolution algorithms (CLEAN and, if warranted, additional selfcal). At the final step, we again insert the disk that was removed, but now this is done in the image plane, not in the uv data.

5.3 The Imaging Pipeline

The imaging pipeline runs automatically every day without direct human intervention. We have standardized on creating full-disk images at 6 frequency bands as shown in Fig. 2.3. The steps in the pipeline, all implemented in CASA, are as follows:

1. Scale the adopted disk sizes according to the Earth-Sun distance relative to what it was on 2019 Sep 03. Write the disk size and flux density information into an xml file for distribution with the subtracted data.
2. Write the model into the model column of the CASA measurement set for all 50 EOVS spectral windows (each of width 325 MHz).
3. Perform two rounds of phase-only selfcal for baselines shorter than $3 \text{ k}\lambda$, one with an infinite window and the second with a one-minute window.
4. Perform one round of amplitude-only selfcal with a scan-length window. The calibration tables from each of these self-calibration runs are concatenated into a single table.
5. Subtract the disk model from the self-calibrated data, and use the residual database to create the images in the 6 standard bands, using multi-frequency synthesis (mfs) on the data with combined spectral windows.
6. Perform multi-scale CLEAN on each of these standard bands to produce final CASA images of disk-subtracted data.
7. Examine the images for peak brightness temperature and if this is sufficiently high (indicating the presence of a strong gyroresonance source), perform additional self-calibration (we call this "feature-selfcal") to improve the calibration of the longer baselines.
8. If feature-selfcal was used, produce new CLEAN images from the corrected database as before.
9. Convert the CASA images to standard solar FITS files, rotated for solar position angle and with a world-coordinate-system (wsc) appropriate to a Sun-centered heliographic system. Write these files as disk-subtracted files.
10. Using the xml file from step 1, add the disk model back in the image plane and write additional FITS files with the disk added.
11. From the disk-added images, produce individual png files for display purposes.

The above procedure results in a set of png files for display (e.g. Fig. 2.3), two sets of FITS files (with and without the disk added), a fully-calibrated, disk-subtracted CASA measurement set, and a calibration table.

You can browse and download these data at <http://ovsa.njit.edu/browser/> (<http://ovsa.njit.edu/browser/>)

or get direct access to the FITS files at http://ovsa.njit.edu/fits/qlook_10m/2019/ (http://ovsa.njit.edu/fits/qlook_10m/2019/)

CASA measurement sets and disk xml files: http://ovsa.njit.edu/fits/UDBms_slfcaled/ (http://ovsa.njit.edu/fits/UDBms_slfcaled/)

6. CONCLUSION

6.1 EOVSAs Capabilities

The Expanded Owens Valley Solar Array is now producing daily full-disk, multi-frequency radio images via its imaging pipeline. This capability is new, and has never been possible before. The spatially-resolved, multi-frequency images reveal the entire range of sources of the solar atmosphere, including compact plage and spotted regions, coronal limb brightening, coronal holes, filaments and prominences, and the (upper) chromosphere.

This entirely new dataset makes it possible to make physical measurements of the solar atmosphere such as global column emission measure maps from free-free emission, as demonstrated here, and also coronal magnetic field maps (not explored here due to space limitations) from gyroresonance emission.

The EOVSAs results compare well with past work, but improve on that work in several ways: (1) the images are available daily, (2) the images are available at many frequencies, (3) the spatial resolution is better than many previous studies. The pipeline produces maps at 6 standard frequencies, but many more are possible, up to 451 frequencies, depending on signal-to-noise considerations.

6.2 Future Prospects

EOVSA is only a 13-antenna demonstrator for a much larger facility called the Frequency Agile Solar Radiotelescope (FASR) that has been highly recommended in several decadal surveys, but not yet realized. The wonderful results shown in this poster are only a taste of what FASR would be able to do with its much higher number of antennas. With FASR's far higher dynamic range and snapshot imaging capability (of order 25 times better), it could make many images per day and follow the temporal evolution of the dynamically changing solar atmosphere. Each image would have far higher quality and sensitivity to faint, large-scale emission, so that the measurements could be taken to higher frequencies.

Figure 6.1 (from Schoenfeld et al. 2015) is an example of what a larger number of antennas can accomplish. This image was obtained with the 27 antennas of the Jansky Very Large Array (JVLA), whose large antennas require that the Sun be imaged in mosaic mode. That limits the speed with which the image can be measured, and also introduces some difficulties in stitching the image together. With 64 antennas, FASR would improve on this image quality by a factor of around 6, and would do so in far less time.

It really is time to fully support the construction of FASR during this coming solar maximum.

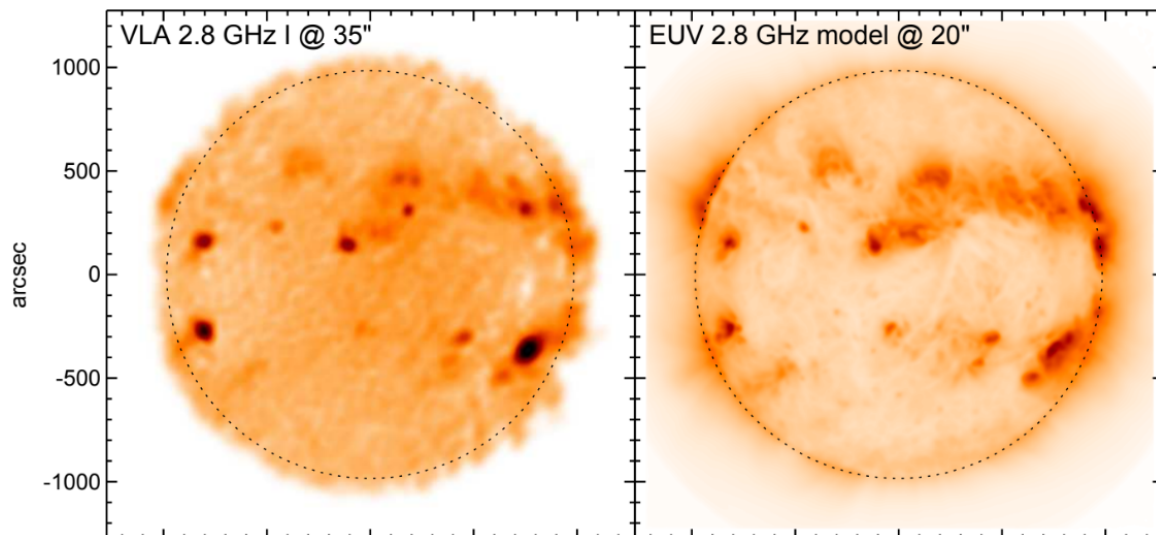


Fig. 6.1: (a) A mosaic image at 2.8 GHz made with the JVLA. (b) A corresponding model for the radio emission based on differential emission measure (DEM) analysis of AIA data. Adapted from Schoenfeld et al. 2015.

You can browse and download these full-disk, multi-frequency images at <http://ovsa.njit.edu/browser/> (<http://ovsa.njit.edu/browser/>)

Acknowledgments: Science and operations of EOVSAs are supported by NSF grant AST-191053 and NASA grants 80NSSC20K0026, 80NNSC19K0068, and 80NNSC181128 to New Jersey Institute of Technology.

REFERENCES

Christiansen, W.N., Warburton, J.A., 1955, "The Distribution of Radio Brightness over the Solar Disk at a Wavelength of 21 Centimetres. III. The Quiet Sun-Two-Dimensional Observations," *Austral. J. Phys.* 8, 474.

Dulk, G.A., 1985, "Radio emission from the sun and stars," *Ann. Rev. Astron. Astrophys.* 23, 169.

Saint-Hilaire, P., Hurford, G. J., Keating, G. Bower, G. C. and Gutierrez-Kraybill, C. 2011, "Allen Telescope Array Multi-Frequency Observations of the Sun," *Solar Physics*, 277, 431

Schonfeld, S. J., White, S. M., Henney, C. J. Arge, C. N. and McAteer, R. T. J. 2015, "Coronal Sources of the Solar F10.7 Radio Flux," *Astrophysical Journal*, 808, 29